

Alma Mater Studiorum Università di Bologna
Archivio istituzionale della ricerca

On the stability of the isoflux Darcy-Bénard problem with a generalised basic state

This is the final peer-reviewed author's accepted manuscript (postprint) of the following publication:

Published Version:

Vayssiere Brandão, P., Barletta, A., Celli, M., Alves, L.S. de B., Rees, D.A.S. (2021). On the stability of the isoflux Darcy-Bénard problem with a generalised basic state. INTERNATIONAL JOURNAL OF HEAT AND MASS TRANSFER, 177, 1-13 [10.1016/j.ijheatmasstransfer.2021.121538].

Availability:

This version is available at: <https://hdl.handle.net/11585/822504> since: 2024-05-23

Published:

DOI: <http://doi.org/10.1016/j.ijheatmasstransfer.2021.121538>

Terms of use:

Some rights reserved. The terms and conditions for the reuse of this version of the manuscript are specified in the publishing policy. For all terms of use and more information see the publisher's website.

This item was downloaded from IRIS Università di Bologna (<https://cris.unibo.it/>).
When citing, please refer to the published version.

(Article begins on next page)

On the stability of the isoflux Darcy–Bénard problem with a generalised basic state

P. V. Brandão^a, A. Barletta^a, M. Celli^a, L. S. De B. Alves^b, D. A. S. Rees^c

^aDepartment of Industrial Engineering, Alma Mater Studiorum Università di Bologna,
Viale Risorgimento 2, 40136 Bologna, Italy.

^bDepartamento de Engenharia Mecânica, Universidade Federal Fluminense,
Rua Passo da Pátria 156, Bloco E, Sala 211, São Domingos, 24210240 Niterói, RJ, Brazil.

^cDepartment of Mechanical Engineering, University of Bath,
Claverton Down, Bath BA2 7AY, United Kingdom.

Abstract

The scope of this study is to determine the conditions for the onset of the instability in a horizontal porous layer subject to isoflux boundary conditions and with an infinitely wide single-cell basic flow. When the circulation in the basic cellular flow is absent, one recovers the usual Darcy–Bénard conduction basic state. The governing parameters are the Rayleigh number associated with the uniform wall heat flux, and the dimensionless horizontal temperature gradient. The latter parameter controls the magnitude of the basic cellular circulation flow in the horizontal direction. The modal analysis of the instability is carried out numerically by employing a pseudo-spectral method, as well as the shooting method for the solution of the stability eigenvalue problem. Neutral stability and the critical conditions for the onset of the convective instability of the basic state are investigated.

Nomenclature

b_1, b_2	roots of the characteristic polynomial, Eq. (19)
\mathcal{B}	matrix of the generalized eigenvalue problem, Eq. (12)
C	positive parameter, Eq. (8)
\mathcal{C}	integration constant
\mathbf{e}_z	unit vector in the z -direction
\mathbf{g}	gravitational acceleration
g	modulus of \mathbf{g}
H	porous layer height
\mathcal{I}_n	expansion coefficient, Eq. (18)
k	wavenumber
K	permeability of the porous medium
\mathcal{L}	linear operator, Eq. (12)
m, n	integers
m_1, \dots, m_4	coefficients, Eq. (A.5)
M_1, \dots, M_4	coefficients, Eq. (A.7)
N	number of collocation points and polynomial order
p	difference between the pressure and the hydrostatic pressure
q	eigenfunctions vector, Eq. (12)
q_0	uniform wall heat flux, Eq. (6)
Ra	Rayleigh number, Eq. (7)
\tilde{Ra}_n	coefficients of the small- C expansion, Eq. (16)

t	time
T_0	reference temperature
T	temperature
\mathbf{u}	velocity vector, (u, v, w)
\mathbf{x}	position vector, (x, y, z)

Greek symbols

α	wave vector component in the x direction, Eq. (9)
β	wave vector component in the y direction, Eq. (9)
γ	thermal expansion coefficient
δ	numerical solver step-size
ΔT	temperature difference, Eq. (4)
ϵ	positive parameter, Figures 2 and 3
ε	perturbation parameter, Eq. (9)
κ	average thermal diffusivity
μ	dynamic viscosity
ρ	density of the fluid for $T = T_0$
σ	volumetric heat capacity ratio
ϕ	inclination between the x axis and the wave vector, Eq. (11)
χ	average thermal conductivity
ω	angular frequency, Eq. (9)

Superscript, subscripts

b	basic state
c	critical value
l	lower
u	upper
$'$	derivative with respect to z
\sim	disturbances eigenfunctions
\wedge	coefficients of the small- k expansions, Eq. (20)

1. Introduction

The onset of thermal instability in a horizontal layer of porous material saturated by a fluid is a topic which has been widely investigated in the literature [1–6]. The instability is of the Darcy–Bénard type where a downward-oriented temperature gradient is built up as the layer is heated from below and the fluid is at rest in the basic state [7]. More complicated versions of the Darcy–Bénard problem have been formulated including uniform heat flux boundary conditions instead of the classical isothermal boundary conditions [5, 8, 9]. The Darcy–Bénard instability with isoflux boundary conditions is characterised by a critical condition at onset where the most unstable modes have a vanishing wavenumber, or infinite wavelength, and a critical Rayleigh number equal to 12 [5, 8].

Another type of thermal instability occurring in a porous layer emerges when a Hadley circulation exists in the basic state [5]. Unlike the Darcy–Bénard system, the Hadley flow involves prescribed boundary temperature distributions with a uniform gradient in a given horizontal direction. The concept of Hadley flow relies on the physics of the atmosphere [10, 11]. The basic mechanism is the existence of a driving horizontal temperature gradient inducing shallow convection cells. The application of this concept in the fluid mechanics of saturated porous media has been investigated in several papers [5, 12–25]. The basic Hadley flow is a bidirectional buoyant flow parametrised by the assigned horizontal temperature gradient. Starting from the pioneering paper by Weber [12], several authors investigated the subject of the transition to instability of the Hadley cell in a saturated porous medium. Usually, the Hadley cell flow in the porous medium is considered as caused by a temperature gradient inclined to the horizontal, so that the Hadley

instability is combined with a Darcy–Bénard instability. Among such studies, Nield [13] took into account the presence of a horizontal pressure gradient altering the Hadley cell flow, while Nield et al. [15] studied the double diffusion due to an imposed solutal gradient. Important results are discussed in the convective and absolute instability analyses carried out by Brevdo and co-workers [21–23] as well as Schuabb et al. [26] for the one and two-dimensional wavepacket dynamics, respectively. Furthermore, the effect of viscous dissipation is analysed in the paper by Barletta and Nield [24], while the heterogeneity of the porous medium is considered in the study carried out by Barletta et al. [25].

The aim of this paper is to revisit the classical Darcy–Bénard problem with uniform heat flux boundary conditions. A one-parameter class of basic states is considered including the classical conduction state where the fluid is at rest as a special case. In particular, it will be shown that the isoflux boundary conditions are compatible with a Hadley flow basic state having an arbitrary horizontal temperature gradient. When such gradient tends to zero, one recovers the classical conduction state of the isoflux Darcy–Bénard problem. This generalised single-cell basic state is parametrised by the Rayleigh number, being proportional to the imposed boundary heat flux, as well as by a horizontal temperature gradient parameter. They are independent parameters in the present study, contrary to the unicellular flows described by Kimura et al. [27]. The stability of these basic states is analysed by employing linearised governing equations for the velocity, pressure and temperature perturbations. The normal mode analysis is employed to carry out the study of the neutral stability conditions. The study is carried out numerically by employing the Chebyshev–Gauss–Lobatto pseudo-spectral method [28–30] and the shooting method [3, 6] for the solution of the stability eigenvalue problem.

2. Mathematical Model

We consider a horizontal porous layer with thickness, H . Coordinate axes are chosen so that the x and y axes are horizontal and the z axis is vertical and directed upward.

The horizontal boundaries are impermeable and subject to the same thermal boundary conditions, that is an upward uniform wall heat flux at both $z = 0$ and $z = H$. In other words, the incoming thermal power at the lower boundary is entirely removed from the upper boundary at each given (x, y) position. The uniform heat flux is modelled by employing Fourier’s law.

2.1. Governing equations

The dimensional governing equations are based on the Oberbeck–Boussinesq approximation and on Darcy’s law, under the assumption that the effect of viscous dissipation is negligible. We will denote with $\mathbf{u} = (u, v, w)$ the velocity, with p the difference between the pressure and the hydrostatic pressure, with T the temperature, and with t the time. Thus, the mass, momentum and heat transport equations [5] can be written as

$$\nabla \cdot \mathbf{u} = 0, \quad (1a)$$

$$\frac{\mu}{K} \mathbf{u} = -\nabla p - \rho \mathbf{g} \gamma (T - T_0), \quad (1b)$$

$$\sigma \frac{\partial T}{\partial t} + \mathbf{u} \cdot \nabla T = \varkappa \nabla^2 T. \quad (1c)$$

The boundary conditions are formulated as

$$z = 0, H : \quad w = 0 \quad \text{and} \quad -\chi \frac{\partial T}{\partial z} = q_0, \quad (2)$$

where γ is the coefficient of thermal expansion of the fluid, g is the modulus of the gravitational acceleration \mathbf{g} , K is the permeability of the porous medium, μ is the fluid dynamic viscosity, \varkappa is the average thermal diffusivity of the saturated porous medium, χ is the average thermal conductivity of the saturated porous medium, ρ is the fluid density, T_0 is the reference temperature, q_0 is the uniform wall heat flux and σ is the ratio between the average heat capacities per unit volume of the saturated porous medium and of the fluid.

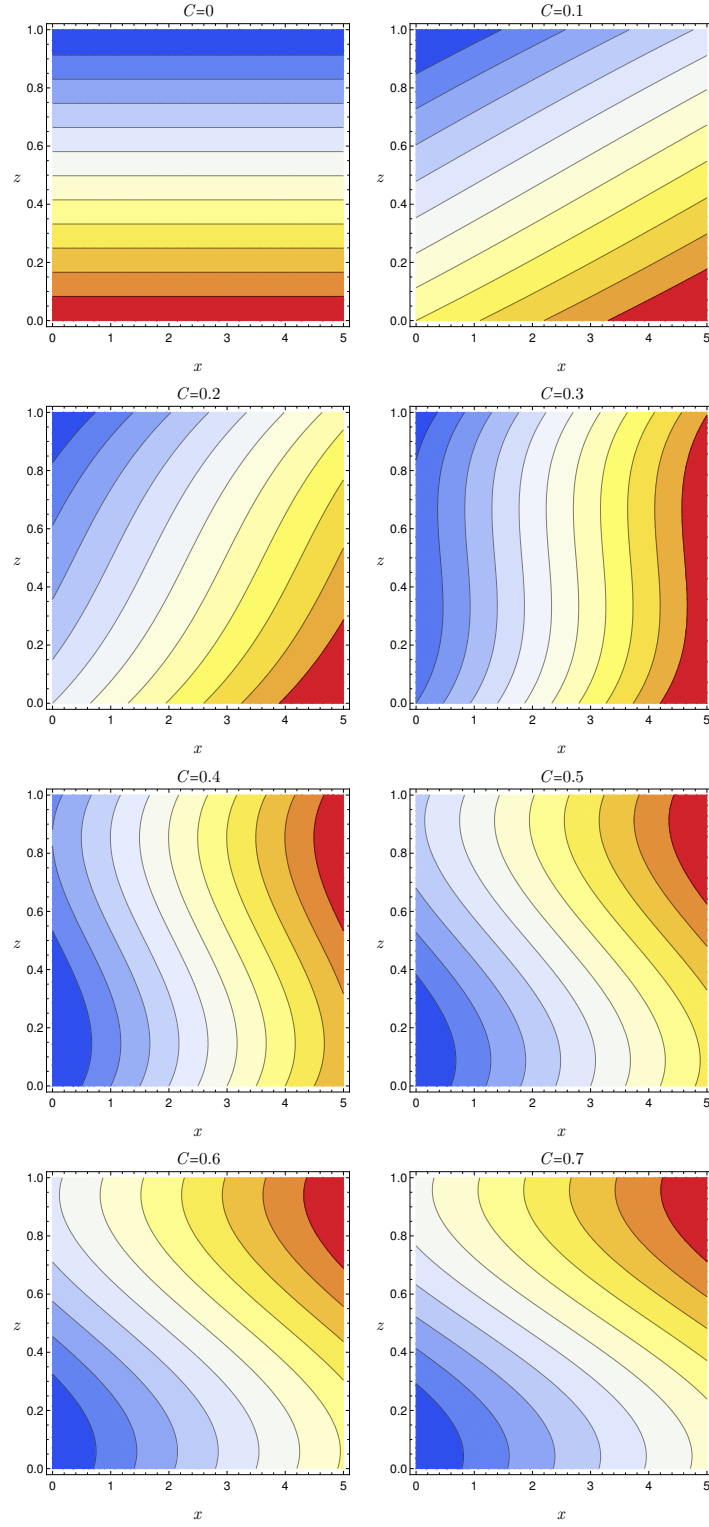


Figure 1: Temperature distribution of the basic solutions characterised by $Ra = 100$: each frame is drawn for different values of C .

By considering the following dimensionless quantities

$$\frac{x}{H} \rightarrow x, \quad t \frac{\varkappa}{\sigma H^2} \rightarrow t, \quad \mathbf{u} \frac{H}{\varkappa} \rightarrow \mathbf{u}, \quad \frac{T - T_0}{\Delta T} \rightarrow T, \quad p \frac{K}{\mu \varkappa} \rightarrow p, \quad (3)$$

where

$$\Delta T = \frac{q_0 H}{\chi}. \quad (4)$$

A dimensionless formulation of the governing equations (1) can be written as

$$\nabla \cdot \mathbf{u} = 0, \quad (5a)$$

$$\mathbf{u} = -\nabla p + Ra T \mathbf{e}_z, \quad (5b)$$

$$\frac{\partial T}{\partial t} + \mathbf{u} \cdot \nabla T = \nabla^2 T, \quad (5c)$$

subjected to the boundary conditions in the dimensionless form

$$z = 0, 1 : \quad w = 0 \quad \text{and} \quad -\frac{\partial T}{\partial z} = 1, \quad (6)$$

where \mathbf{e}_z is the unit vector along the z axis. The Rayleigh number Ra is defined as

$$Ra = \frac{\rho \gamma g \Delta T K H}{\mu \varkappa}. \quad (7)$$

2.2. Basic solution

A stationary solution of Eqs. (5) subject to the boundary conditions (6) is given by

$$u_b = -Ra C \left(z - \frac{1}{2} \right), \quad v_b = 0, \quad w_b = 0, \quad (8a)$$

$$T_b = C x - \frac{1}{12} z [12 - Ra C^2 (3 - 2z) z] + \text{constant}, \quad (8b)$$

$$\frac{\partial p_b}{\partial x} = -u_b, \quad \frac{\partial p_b}{\partial y} = 0, \quad \frac{\partial p_b}{\partial z} = Ra T_b. \quad (8c)$$

Here, the subscript b indicates the basic solution, while C is an arbitrary constant which controls the intensity of the horizontal flow and of the temperature gradient in the x direction. We note that, on account of Eqs. (8), the horizontal flow rate is zero. In fact, for any given Rayleigh number Ra , Eqs. (8) define a one-parameter class of parallel flow solutions of the governing equations by varying the value of the constant C . In the limit $C \rightarrow 0$, we recover the basic state of the isoflux Darcy–Bénard problem analysed by Nield [8] and surveyed in chapter 6 of Nield and Bejan [5]. A sign change of the constant C does not imply any important change in the physical meaning of the solution as it can be compensated by a reflection of the x axis. In the following, we will focus on non-negative values of C . We point out that, due to the isoflux boundary conditions, the temperature T_b is defined only up to an arbitrary additive constant which, however, has no impact on the stability analysis. Figure 1 shows plots of the isotherms $T_b = \text{constant}$ for the case $Ra = 100$ with different values of C . The case where $C = 0$ yields straight horizontal isotherms meaning that the temperature gradient is purely vertical. As already pointed out above, this is the special case where the basic state is that corresponding to the classical Darcy–Bénard problem. When $C > 0$, the temperature gradient is not purely vertical and it gradually becomes less and less uniform. Equations (8) show that, in the asymptotic regime where $C \gg 1$, the x component of the temperature gradient becomes dominant close to the boundaries at $z = 0, 1$, while the z component of the temperature gradient is dominant close to the midplane $z = 1/2$.

We point out that the solution (8) formally coincides with that discussed by Kimura et al. [27] and, more recently, by Gueye et al. [31]. Despite the formal congruence of such solutions, their physical meaning is utterly different. In fact, both Kimura et al. [27] and Gueye et al. [31] assume that Eqs. (8) are meant to describe the parallel flow in the central core of a single cell formed within a shallow rectangular cavity. The vertical sidewalls of the cavity, placed at suitable $x = \text{constant}$ positions, are considered as adiabatic [27, 31]. The adiabaticity constraint induces a relationship between the parameters C and Ra , so that these parameters cannot be varied independently. Our analysis relaxes the adiabaticity constraints for the sidewalls. Since the single cell flow (8) is to be intended as the core flow within a rectangular cavity having an infinitely large horizontal width, vertical cavity sidewalls are not modelled in any way within our analysis. This independence can be established in alternative ways as well. For instance, Kalla et al. [32] assume that the vertical sidewalls are subject to isoflux conditions with a nonzero wall heat flux. As a consequence, they establish an independence of the parameters C and Ra induced by a third governing parameter associated with the sidewall heat flux. Thus, our study assumes no relationship between the parameters C and Ra , so that these parameters will be considered as independent in the forthcoming stability analysis.

3. Linear stability analysis

In order to carry out the linear stability analysis, we assume that the basic flow given by Eqs. (8) is perturbed by small-amplitude disturbances defined as normal modes, namely

$$\begin{aligned} \mathbf{u}(x, y, z, t) &= \mathbf{u}_b(z) + \varepsilon \tilde{\mathbf{u}}(z) e^{i(\alpha x + \beta y - \omega t)}, \\ p(x, y, z, t) &= p_b(x, z) + \varepsilon \tilde{p}(z) e^{i(\alpha x + \beta y - \omega t)}, \\ T(x, y, z, t) &= T_b(x, z) + \varepsilon \tilde{T}(z) e^{i(\alpha x + \beta y - \omega t)}, \end{aligned} \quad (9)$$

where ε is a small perturbation parameter, α and β are, respectively, the real components of the wave vector in the streamwise and spanwise directions, ω is the complex frequency and $\tilde{u}(z)$, $\tilde{v}(z)$, $\tilde{w}(z)$ and $\tilde{T}(z)$ are the eigenfunctions. By substituting Eq. (9) into Eqs. (5) and (6), as well as neglecting terms of $O(\varepsilon^2)$, one obtains the linearised equations governing the evolution of the infinitesimal disturbances. Moreover, by applying the curl operator on the momentum balance equation we can get rid of the pressure field, so that we can express the linearised disturbance equations in the following way:

$$\tilde{w}'' - k^2 (\tilde{w} - Ra \tilde{T}) = 0, \quad (10a)$$

$$\begin{aligned} \tilde{T}'' - \left[k^2 - ik \cos \phi Ra C \left(z - \frac{1}{2} \right) - i\omega \right] \tilde{T} \\ + \left[1 - \frac{1}{2} Ra C^2 (1 - z) z \right] \tilde{w} - \frac{iC \cos \phi}{k} \tilde{w}' = 0, \end{aligned} \quad (10b)$$

$$z = 0, 1 : \quad \tilde{w} = 0 = \tilde{T}', \quad (10c)$$

where the wavenumber k and the components of the wave vector can be expressed as

$$k = \sqrt{\alpha^2 + \beta^2}, \quad \alpha = k \cos \phi, \quad \beta = k \sin \phi. \quad (11)$$

The angle ϕ yields the inclination between the x axis and the direction of the wave vector, with $0 \leq \phi \leq \pi/2$. In the first instance, problem (10) is solved for the neutral stability condition, with given values of C and ϕ . For every value of the wavenumber, k , one has the corresponding value of Ra that satisfies the condition of zero growth rate. The pairs (k, Ra) defining the neutral stability condition yield the neutral stability curve. The critical condition is obtained by seeking the minimum value of Ra along the neutral stability curve. Thus, for every pair of input parameters (C, ϕ) , one can determine the critical values (k_c, Ra_c) . Details about the shooting method used to solve the stability eigenvalue problem and generate the neutral stability curves as well as their critical values (k_c, Ra_c) can be found, for instance, in Straughan [3] and in Barletta [6].

3.1. Matrix formulation

A well-known drawback of the shooting method is the impracticality of an automatic routine to detect all possible eigenvalue branches while solving Eqs. (10). An alternative numerical approach filling this gap is based on a matrix reformulation of the differential eigenvalue problem (10). The main advantage of a matrix-forming approach is that it aims to obtain the entire (truncated) spectrum of the linear operator in a single sweep of (k, Ra) -space. In fact, we can rewrite the eigenvalue problem (10) as

$$\mathcal{L}q = \omega \mathcal{B}q, \quad (12)$$

where \mathcal{L} and \mathcal{B} are linear operators, q is the vector formed by \tilde{w} and \tilde{T} and ω is the complex eigenvalue. Equation (12) can be reformulated as

$$\begin{bmatrix} \mathcal{L}_{11} & \mathcal{L}_{12} \\ \mathcal{L}_{21} & \mathcal{L}_{22} \end{bmatrix} \begin{bmatrix} \tilde{w} \\ \tilde{T} \end{bmatrix} = \omega \begin{bmatrix} \mathcal{B}_{11} & \mathcal{B}_{12} \\ \mathcal{B}_{21} & \mathcal{B}_{22} \end{bmatrix} \begin{bmatrix} \tilde{w} \\ \tilde{T} \end{bmatrix}, \quad (13)$$

where

$$\begin{aligned} \mathcal{L}_{11} &= D^2 - k^2 I, & \mathcal{L}_{12} &= k^2 Ra I, \\ \mathcal{L}_{21} &= \left[1 - \frac{1}{2} Ra C^2 (1 - z) z \right] I - \frac{iC \cos \phi}{k} D, \\ \mathcal{L}_{22} &= D^2 - \left[k^2 - ik \cos \phi Ra C \left(z - \frac{1}{2} \right) \right] I, \end{aligned} \quad (14)$$

where I is the identity matrix, D is the matrix corresponding to the differential operator d/dz and

$$\mathcal{B}_{11} = 0, \quad \mathcal{B}_{12} = 0, \quad \mathcal{B}_{21} = 0, \quad \mathcal{B}_{22} = -i I. \quad (15)$$

The matrix-forming approach adopted here is the Chebyshev–Gauss–Lobatto pseudo-spectral method described in Boyd [28], Juniper et al. [29] and El-Baghdady and El-Azab [30]. The differential eigenvalue problem then becomes an algebraic eigenvalue problem which can be solved in different ways. In this study, the QZ algorithm from the Fortran library *Linear Algebra PACKage* (LAPACK) [33] is used.

4. Asymptotic analysis for small values of C

It is worth noting that when $C = 0$ the classical basic state is recovered and, therefore, it is of some interest to investigate the deviation from this state when C takes on small values. When $C = 0$ it is possible to recover an analytical solution.

If one considers just longitudinal modes ($\phi = \pi/2$), Eqs. (10) reveal that the eigenvalue problem depends on C^2 , so that we can write the expansions

$$\tilde{w} = \sum_{n=0}^{\infty} \tilde{w}_n C^{2n}, \quad \tilde{T} = \sum_{n=0}^{\infty} \tilde{T}_n C^{2n}, \quad Ra = \sum_{n=0}^{\infty} \tilde{Ra}_n C^{2n}. \quad (16)$$

At each order j , substitution of Eq. (16) into Eqs. (10) yields

$$\begin{aligned} \tilde{w}_n'' - k^2 \tilde{w}_n + k^2 \sum_{m=0}^n \tilde{Ra}_m \tilde{T}_{n-m} &= 0, \\ \tilde{T}_n'' - k^2 \tilde{T}_n + \tilde{w}_n - \mathcal{I}_n &= 0, \end{aligned} \quad (17)$$

where $\mathcal{I}_0 = 0$ and

$$\mathcal{I}_n = -\frac{1}{2} z(1 - z) \sum_{m=0}^{n-1} \tilde{Ra}_m \tilde{w}_{n-m-1}, \quad (18)$$

for $n > 1$.

At zero order, we have the implicit expression for the solution of $\tilde{R}a_0$

$$k^2 \sinh(b_1) \sinh(b_2) + b_1 b_2 [\cosh(b_1) \cosh(b_2) - 1] = 0, \quad (19)$$

that depends on k , where $b_1 = \left(k^2 - k\tilde{R}a_0^{1/2}\right)^{1/2}$ and $b_2 = \left(k^2 + k\tilde{R}a_0^{1/2}\right)^{1/2}$.

At second and fourth orders, it is possible to obtain an explicit solution for both $\tilde{R}a_1$ and $\tilde{R}a_2$. They are, however, very lengthy expressions and, hence, will be omitted here.

5. Asymptotic analysis for small values of k

It is well-known in the literature that when $C = 0$ the critical Rayleigh number $Ra_c = 12$ occurs at $k_c = 0$. Hence, by undertaking an asymptotic analysis as $k \rightarrow 0$ it is possible to determine how the critical Rayleigh number is affected by variations in C . For the present case we shall work with the original equations (10). Expanding the variables as power series in k leads to

$$\tilde{w} = \sum_{n=0}^{\infty} \hat{w}_n k^n, \quad \tilde{T} = \sum_{n=0}^{\infty} \hat{T}_n k^n, \quad Ra = \sum_{n=0}^{\infty} \hat{R}a_n k^n. \quad (20)$$

The solutions at each order are,

$$\hat{w}_0 = 0, \quad (21a)$$

$$\hat{T}_0 = 1, \quad (21b)$$

$$\hat{w}_1 = 0, \quad (21c)$$

$$\hat{T}_1 = C_1 - \frac{1}{6}i C \hat{R}a_0 z^2 (2z - 3) \cos(\phi), \quad (21d)$$

$$\hat{w}_2 = -\frac{1}{2}\hat{R}a_0(z-1)z, \quad (21e)$$

$$\hat{w}_3 = \frac{1}{120}iz(z-1)[60i(C_1\hat{R}a_0 + \hat{R}a_1) + C\hat{R}a_0^2(2z^3 - 3z^2 - 3z - 3)\cos(\phi)], \quad (21f)$$

which lead to find the solution of \hat{T}_2 up to an additional integration constant,

$$\begin{aligned} \hat{T}_2 = \frac{1}{1440} \big[& 720z^2 - 9C^2\hat{R}a_0^2z^2 - 120\hat{R}a_0z^3 + 60\hat{R}a_0z^4 + \\ & 15C^2\hat{R}a_0^2z^4 - 6C^2\hat{R}a_0^2z^5 + 2C^2\hat{R}a_0^2z^6 + 1440C_2 - \\ & C^2\hat{R}a_0^2z^2(9 + 15z^2 - 30z^3 + 10z^4)\cos(2\phi) - \\ & 240iC(C_1\hat{R}a_0 + \hat{R}a_1)z^2(2z - 3)\cos(\phi) \big]. \quad (22) \end{aligned}$$

After applying the boundary condition, $\hat{T}_2'(1) = 0$, the resulting quadratic equation for $\hat{R}a_0$ provides the following two solutions,

$$\hat{R}a_0^l = \frac{120}{\sqrt{5}\sqrt{5 - 24C^2\cos(2\phi)} - 48C^2 + 5}, \quad (23)$$

$$\hat{R}a_0^u = -\frac{120}{\sqrt{5}\sqrt{5 - 24C^2\cos(2\phi)} - 48C^2 - 5}, \quad (24)$$

where the superscripts, l and u , refer to lower and upper, respectively.

Two important remarks must be made at this point. The first is that, in the limit $C \rightarrow 0$, we have $\hat{R}a_0^l \rightarrow 12$ and $\hat{R}a_0^u \rightarrow \infty$, in accordance with the classical results for $C = 0$. The second is that physically

sensible results correspond to positive values of the argument of the square roots. This means that C must satisfy the inequalities

$$-\frac{\sqrt{5}}{2\sqrt{6(2+\cos(2\phi))}} < C < \frac{\sqrt{5}}{2\sqrt{6(2+\cos(2\phi))}}. \quad (25)$$

Given that the stability problem is essentially unchanged for negative values of C this means that we may restrict this condition to positive values, hence C satisfies,

$$C < \frac{\sqrt{5}}{2\sqrt{6(2+\cos(2\phi))}}. \quad (26)$$

If this condition is violated then we conclude that there is no solution for which for $k = 0$. This limit represents for instance

$$C < \frac{\sqrt{5}}{6\sqrt{2}} \sim 0.263523, \quad (27)$$

for $\phi = 0$, and

$$C < \frac{\sqrt{5}}{2\sqrt{6}} \sim 0.456435, \quad (28)$$

for $\phi = \pi/2$.

6. Discussion of the results

6.1. Verification

In this section we present the convergence analysis of the numerical calculations as well as a verification of the results by comparing both numerical approaches considered. Table 1 and 2 show the convergence of the calculation performed in the *Mathematica* environment for the first and second most unstable modes, respectively. The built-in function `NDSolve` works with an adaptive step-size mesh by default, so decreasing fixed step-size mesh results were obtained as well and compared with the ones obtained from the adaptive one. All results shown in tables 1 and 2 consider ω as the unknown variable while the other parameters are imposed. It can be seen that the adaptive mesh returns highly accurate results.

Figures 2 and 3, on the other hand, show the convergence of the numerical calculations performed with the pseudo-spectral Chebyshev-Gauss-Lobatto method. As expected for a pseudo-spectral method, convergence rates are high and the absolute error reaches a minimum for a small number of mesh points. This error was calculated using as a reference solution the adaptive mesh shooting method results.

δ	$\text{Re}[\omega]$	$\text{Im}[\omega]$
0.1	76.1301413428	71.3389808444
0.05	76.3608999828	71.5537897173
0.025	76.3759942723	71.5688304389
0.0125	76.3768763616	71.5698331905
0.01	76.3769093734	71.5698737008
0.005	76.3769304117	71.5699002616
0.0025	76.3769316885	71.5699019385
0.00125	76.3769317671	71.5699020438
Adaptive	76.3769317723	71.5699020508

Table 1: Shooting method convergence: a comparison of the results obtained for different values of the fixed step-size δ employed for the domain discretization. The values of the angular frequency ω are obtained for $C = 0.1$, $\phi = 0$, $Ra = 600$, $k = 5$ and for the most unstable mode.

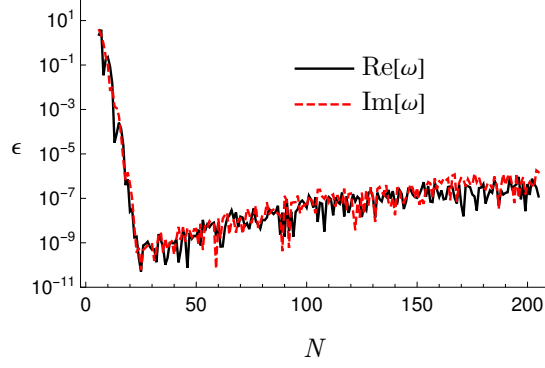


Figure 2: Absolute value ϵ of the difference between the results obtained by employing the pseudo-spectral method and the shooting method with adaptive step-size mesh. The parameter ϵ is plotted for different values of the number of collocation points N as well as the order of the Chebyshev polynomial. The values of the angular frequency ω are obtained for $C = 0.1$, $\phi = 0$, $Ra = 600$, $k = 5$ and for the first most unstable mode.

δ	$\text{Re}[\omega]$	$\text{Im}[\omega]$
0.1	38.2012727048	-43.2049433605
0.05	38.5648973811	-43.5971821585
0.025	38.5954461409	-43.6186157267
0.0125	38.5975837099	-43.6197805121
0.01	38.5976713085	-43.6198220187
0.005	38.5977289672	-43.6198479227
0.0025	38.5977326243	-43.6198494454
0.00125	38.5977328544	-43.6198495374
Adaptive	38.5977328698	-43.6198495434

Table 2: Same as Table 1 but for the second most unstable mode.

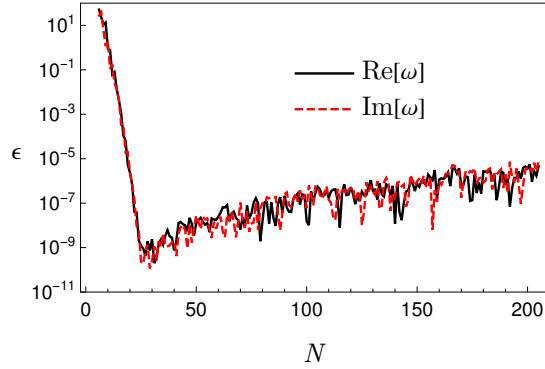


Figure 3: Same as Figure 2 but for the second most unstable mode.

All results shown from now on were obtained with the adaptive step-size mesh shooting method and the pseudo-spectral method with $N = 21$. Figure 4 presents a comparison between the results obtained with both methods. One can observe a good agreement between them, as already expected from the convergence analysis.

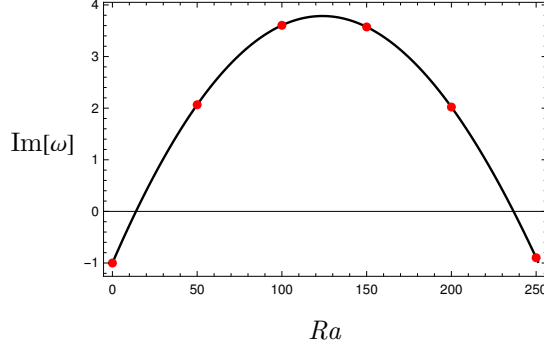


Figure 4: Growth rate as a function of Ra for $C = 0.2$, $\phi = \pi/2$ and $k = 1$: comparison between shooting method (continuous line) and matrix forming (red dots) results.

Now that the accuracy of the numerical results has been verified, it is possible to compare these results with those from the asymptotic analysis for small values of C . Such an analysis can be quite useful because the C parameter cannot assume high magnitudes. Table 3 shows the comparison between the neutral stability Ra calculated with the shooting method and those from the asymptotic analysis, considering the zeroth, second and fourth order approximations. Consistent trends can be observed.

C	Ra	\tilde{Ra}_0	$\tilde{Ra}_0 + C^2 \tilde{Ra}_1$	$\tilde{Ra}_0 + C^2 \tilde{Ra}_1 + C^4 \tilde{Ra}_2$
0.001	16.5065313573078	16.5065039553139	16.5066197841567	16.5066197853894
0.01	16.5092450551770	16.5065039553139	16.5180868395888	16.5180991675637
0.05	16.5755829985049	16.5065039553139	16.7960760621851	16.7368123770508
0.1	16.7900117639327	16.5065039553139	17.6647923827987	16.7165734205878

Table 3: Comparison between the Rayleigh number Ra obtained by employing the shooting method and the Rayleigh number obtained by employing the asymptotic analysis for small values of C truncated at zeroth (\tilde{Ra}_0), second ($\tilde{Ra}_0 + C^2 \tilde{Ra}_1$), and fourth ($\tilde{Ra}_0 + C^2 \tilde{Ra}_1 + C^4 \tilde{Ra}_2$) orders. The values of the Rayleigh number are obtained for $k = 2$ and $\phi = \pi/2$.

6.2. Discussion

In this section we will present and discuss the stability results, focusing on the influence of C and ϕ on neutral stability curves and their respective critical points and most unstable modes. Figure 5 shows the neutral stability curves for different values of ϕ . The most unstable curve for each inclination angle is the one corresponding to $C = 0$. As the value of C increases from zero, the region enclosed by these curves shrinks, becoming finite, and eventually disappears, indicating the appearance of an upper bound for instability. This trend is observed for longitudinal, oblique and transverse modes.

Figure 6 shows the neutral stability curve for $C = 0$, whose critical point is known to be $Ra_c = 12$ and $k_c = 0$. It is worth mentioning that there is no preferred direction for the disturbance in this case and, therefore, the results do not depend on ϕ .

The effect of C and ϕ is now going to be carefully investigated for three specific points, marked on the neutral curve in Fig. 6. Figure 7 shows how the marginal Ra for each one of these wavenumbers changes as C varies when $\phi = \pi/2$. In all three cases, there is a maximum value of C above which the flow is stable. Smaller k values correspond to larger maximum C values and smaller corresponding marginal Ra values, suggesting once again that Ra_c is obtained in the limit as $k \rightarrow 0$. Such a result indicates that, as C increases, the unstable region in (k, Ra) -space shrinks until it disappears. It also agrees with the asymptotic analysis for $k \rightarrow 0$, which says through Eq. (26) that, for each value of ϕ , there exists a maximum value of C for which the neutral stability result holds. In Figs. 7 and 8 the dashed black lines are relative to the analytical solution from the asymptotic analysis, given by Eqs. (23) and (24). A good agreement can be observed

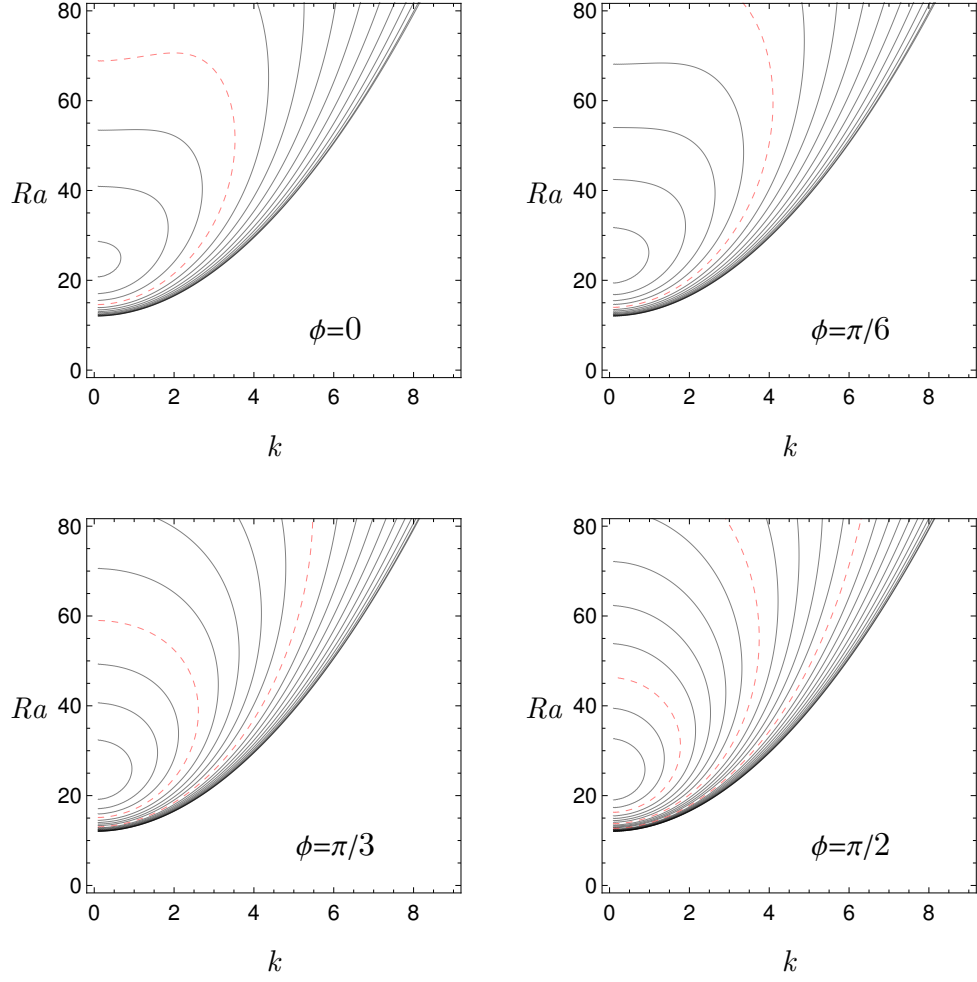


Figure 5: Neutral stability curves for different values of C , in steps of 0.02, starting from $C = 0$ up to $C = 0.26, 0.28, 0.36$ and 0.44 for $\phi = 0, \pi/6, \pi/3$ and $\pi/2$, respectively. Red curves indicate those relative to $C = 0.2, 0.3, 0.4$.

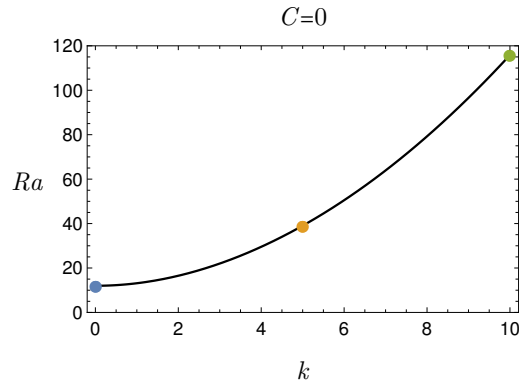


Figure 6: Neutral stability curve for $C = 0$. The coloured points define the three wavenumbers, $k = 0.01, 5, 10$, employed in the detailed investigation of the influence of C and ϕ on the neutral stability curve.

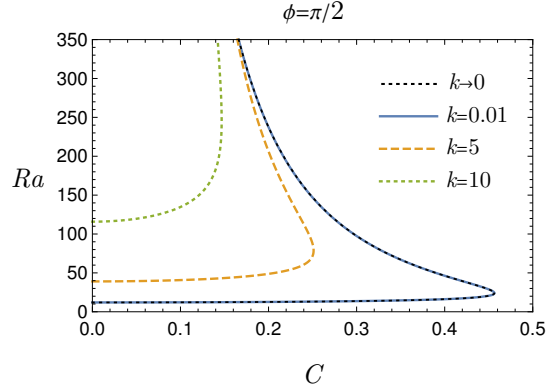


Figure 7: Rayleigh number as a function of C for different values of k and $\phi = \pi/2$. Neutrally stable modes are considered.

between the numerical solution for $k = 0.01$ and the asymptotic analytical solution for $k \rightarrow 0$. Such a good agreement also provides a further verification of the numerical method.

Now that the maximum C value beyond which the flow is stable has been found for $\phi = \pi/2$, its behaviour with respect to smaller ϕ is investigated and presented in Fig. 8 for the same three wavenumbers marked in Fig. 6. This figure shows the maximum C value monotonically decreases with respect to C . Hence, longitudinal modes are the most unstable. This is an expected results based on the inequalities presented in Eqs. (27) and (28).

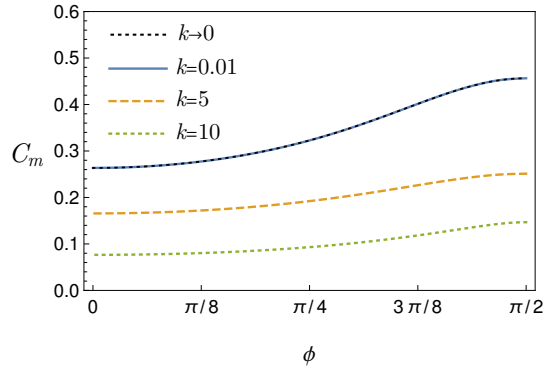


Figure 8: Maximum value of C , for fixed k and ϕ , beyond which no neutrally stable modes are possible.

Figure 9 shows a three-dimensional map of the most unstable mode for $C = 0.1$, containing its growth rate as a function of the wave and Rayleigh numbers for $\phi = 0$ (left) and $\phi = \pi/2$ (right). This growth rate is qualitatively different in both cases. While there is an abrupt change in the dominant mode at a certain line $f(k, Ra) = \omega_1(k, Ra) - \omega_2(k, Ra) = 0$ when $\phi = 0$, no such thing occurs when $\phi = \pi/2$. Subscripts 1 and 2 represent the first and second dominant modes. In order to understand the reason for this qualitative change in behaviour with respect to ϕ , a cross-section for a fixed value of k in both three-dimensional maps is investigated in detail. Figures 10 and 11 show frequency data along such a cross-section, namely for $k = 5$, illustrated by the black line in Fig. 9 for $\phi = 0$ (left) and $\phi = \pi/2$ (right), respectively.

Let us first consider Fig. 10. It shows a synchronization of the two most unstable modes as Ra increases along $k = 5$. As shown in Fig. 10 (top left), two unstable modes exist when Ra is large enough but still $Ra < Ra_m$, where $f(k = 5, Ra_m) = 0$. They are shown as solid and dashed lines in this figure. Furthermore, they are both stationary, as shown in Fig. 10 (top right). In other words, both modes have the same frequency but different temporal growth rates. This scenario changes at $Ra = Ra_m$, where these two modes

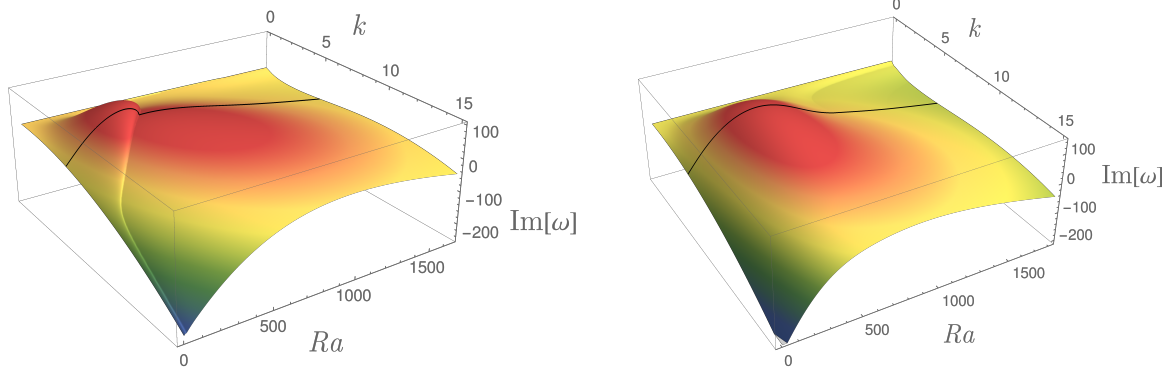


Figure 9: Three dimensional map showing the growth rate as a function of the wave and Rayleigh numbers for $C = 0.1$ with $\phi = 0$ (left) and $\phi = \pi/2$ (right).

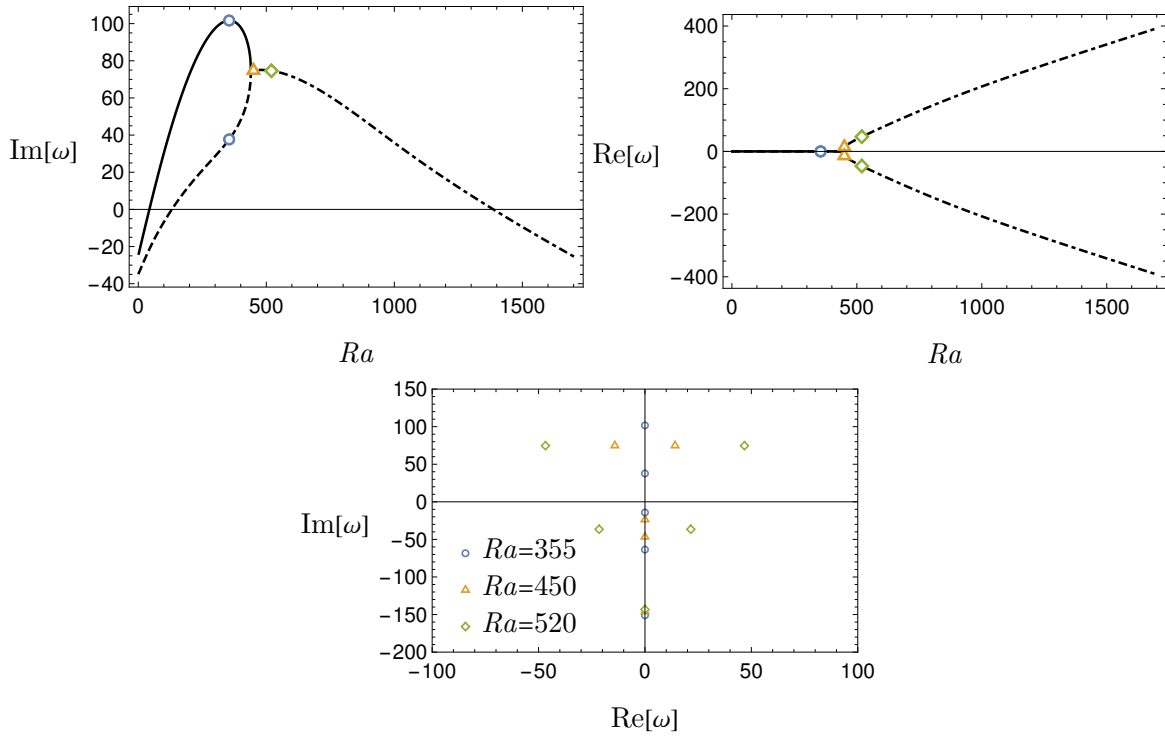


Figure 10: Temporal growth rate (top left) and frequency (top right) as functions of Ra as well as the frequency spectra at three different Ra (bottom). Data obtained for $k = 5$, $C = 0.1$ and $\phi = 0$. Solid and dashed lines represent most unstable modes before synchronization at $Ra_m \simeq 438.110$. Dot dashed lines represents both modes beyond this point.

synchronize. Beyond this point, Fig. 10 (top left) shows that both modes are equally unstable, remaining so as long as Ra is not too large but stable otherwise. They are illustrated by the dot dashed line in this figure. Furthermore, they have now become travelling modes, with phase speeds that are equal in magnitude but opposite in direction. In other words, both modes have the same temporal growth rate but different frequencies. This behaviour change is presented through a different perspective through Fig. 10 (bottom), which shows the spectra at three different Ra around the synchronization point at $Ra_m \simeq 438.110$.

Figure 11 is considered next. It shows similar data to Fig. 10, but for $\phi = \pi/2$. Under these conditions, however, synchronization does not occur. Both modes have different temporal growth rates, as shown in

Fig. 11 (left), and remain stationary, as shown in Fig. 11 (right), as Ra is increased. Nevertheless, it is interesting to note that their temporal growth rates do become quite close beyond a high enough Ra , even though synchronization does not occur. This behaviour change is summarized in Fig. 11 (bottom), which shows the spectra at three different Ra within this high Ra region. Hence, synchronization occurs for transverse modes ($\phi = 0$) but not for longitudinal ones ($\phi = \pi/2$).

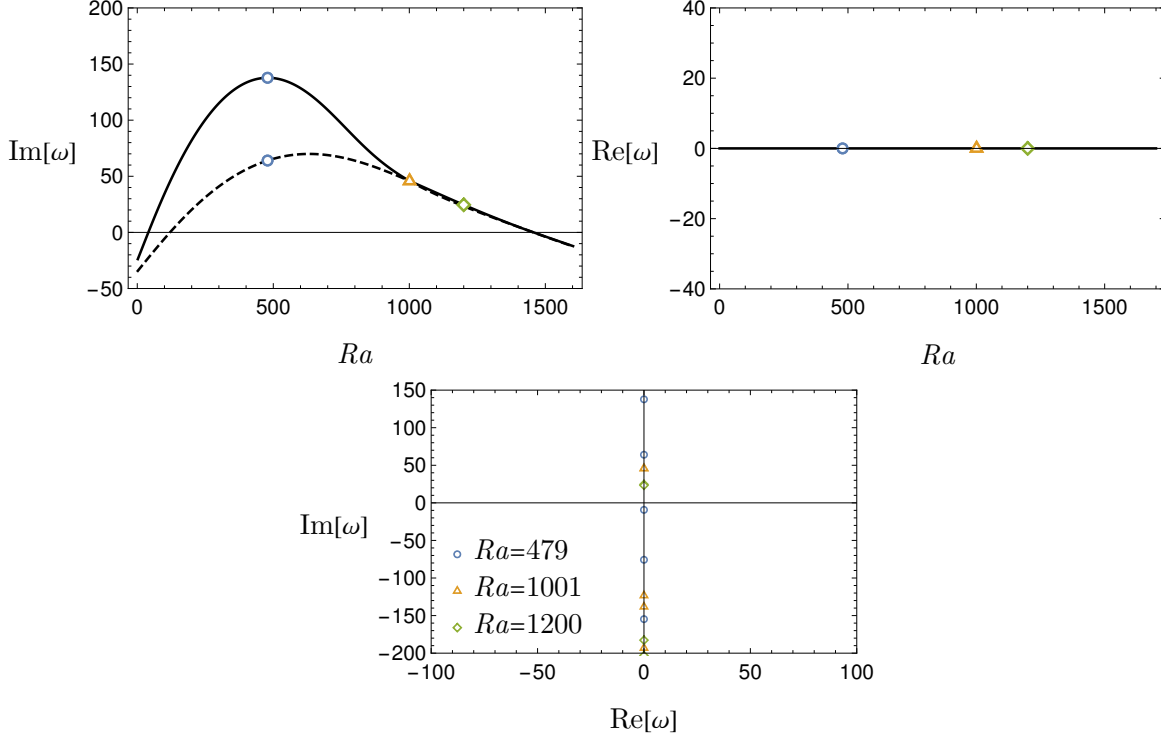


Figure 11: Same as Fig. 10, but for $\phi = \pi/2$. No synchronization occurs.

It is now possible to investigate the influence of C on the results presented so far. There is no preferred orientation of the wave vector when $C = 0$. On the other hand, these results are greatly affected by ϕ when $C > 0$. Figures 12 and 13 show neutral stability curves for different values of C for transverse ($\phi = 0$) and longitudinal ($\phi = \pi/2$) modes, respectively. Positive temporal growth rate isocontours (thin lines) are displayed within each neutral stability curve (thick solid lines), where the synchronization line $f(k, Ra) = 0$ (thick dashed lines) is also shown whenever present. Since a finite parametric region of instability exists when $C > 0$, there are lower and upper bounds for the critical Rayleigh number as well as a global maximum temporal growth rate, which is indicated by a red dot. It is obtained by an optimization process of the original problem with respect to Ra and k very similar to the automatic critical point search employed in a previous work [34]. The additional equations required for this procedure are obtained by taking derivatives of Eqs. (10) with respect of both Ra and k and then imposing $\partial \text{Im}[\omega] / \partial Ra = 0$ and $\partial \text{Im}[\omega] / \partial k = 0$. Further details can be found elsewhere [6, 35].

Four important qualitatively similar trends between both cases, namely $\phi = 0$ and $\pi/2$, are discussed first. One is the fact that the lower bound for the critical Rayleigh number always occurs at $k = 0$, can be analytically determined by Eq. (23) and is associated with the first dominant mode shown in Figs. 10 and 11 when $C > 0$. Another is the fact that all most unstable supercritical modes are nonuniform, i.e. they have $k > 0$, including the most unstable mode represented by a red dot in Figs. 12 and 13. Hence, nonlinear saturation is unlikely to be first reached by the transitional uniform mode in the supercritical region. Nevertheless, such an analysis is beyond the scope of the present work. Yet another trend is the fact that the upper bound for the critical Rayleigh number only occurs at $k = 0$ when C is large enough. Under

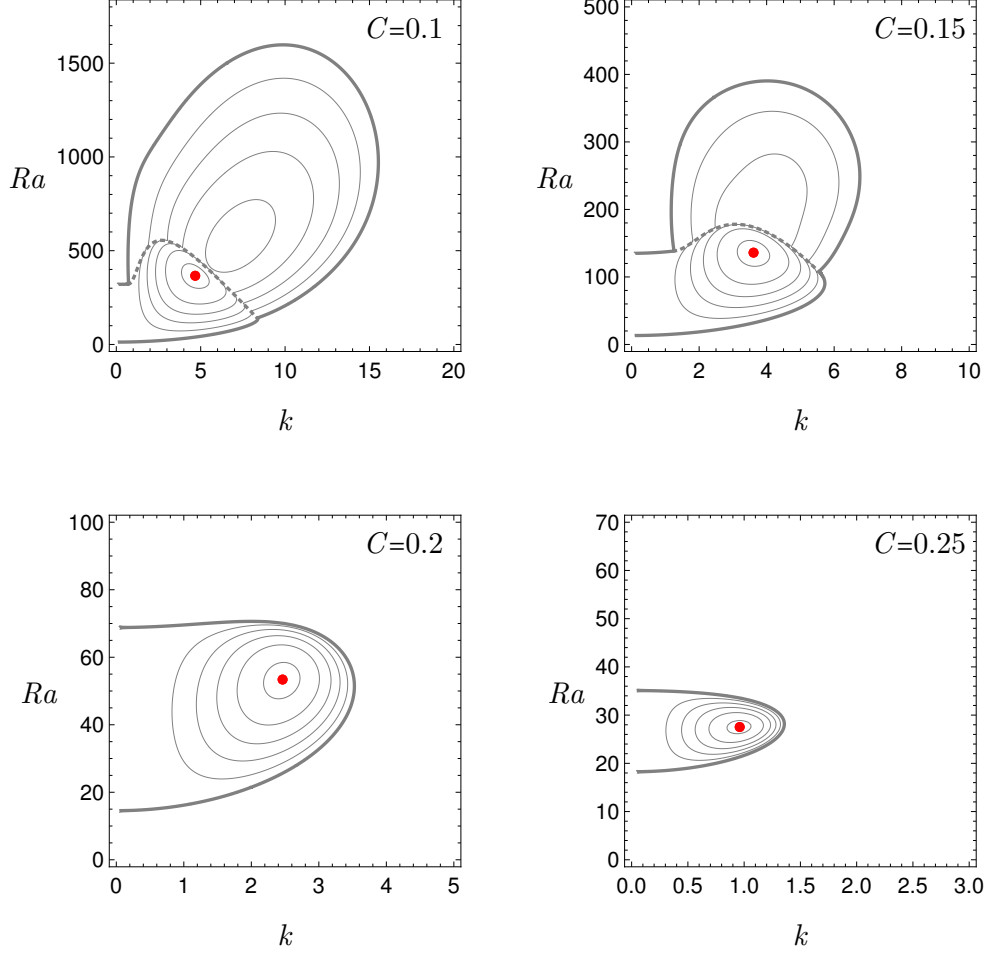


Figure 12: Neutral stability curves (thick solid lines) and temporal growth rate isolines (thin solid lines) for different values of C with $\phi = 0$. The red dots identify the maximum temporal growth rate: $\text{Im}[\omega] = 102.298$ at $Ra = 366.298$ and $k = 4.6754$ for $C = 0.1$, $\text{Im}[\omega] = 21.7067$ at $Ra = 135.978$ and $k = 3.61197$ for $C = 0.15$, $\text{Im}[\omega] = 2.58776$ at $Ra = 53.3939$ and $k = 2.46325$ for $C = 0.2$ and $\text{Im}[\omega] = 0.0515489$ at $Ra = 27.5296$ and $k = 0.960554$ for $C = 0.25$.

these parametric conditions, it is determined by Eq. (24). Otherwise, it occurs at $k > 0$. The fourth and final trend is that Figs. 12 and 13 qualitatively confirm the maximum values of C beyond which the flow is no longer unstable for $\phi = 0$ and $\pi/2$, respectively given by Eqs. (27) and (28).

Three important qualitatively distinct trends between these same cases, namely $\phi = 0$ and $\pi/2$, are now discussed. One is that lower and upper onsets of instability occur through longitudinal modes. Furthermore, they are the most unstable within the supercritical region as well, since their maximum temporal growth rates are always higher than that of transverse modes for the same C . Another is that longitudinal modes are stationary for any C , but the same is true for transverse modes only at a small enough C . Otherwise the latter become travelling modes due to the mode synchronization phenomenon. This phenomenon is also associated with the third and final distinct trend. The transverse mode temporal growth rate has two local maxima with respect to k for a small enough C , whereas the respective longitudinal mode curve has a single global maximum for any C .

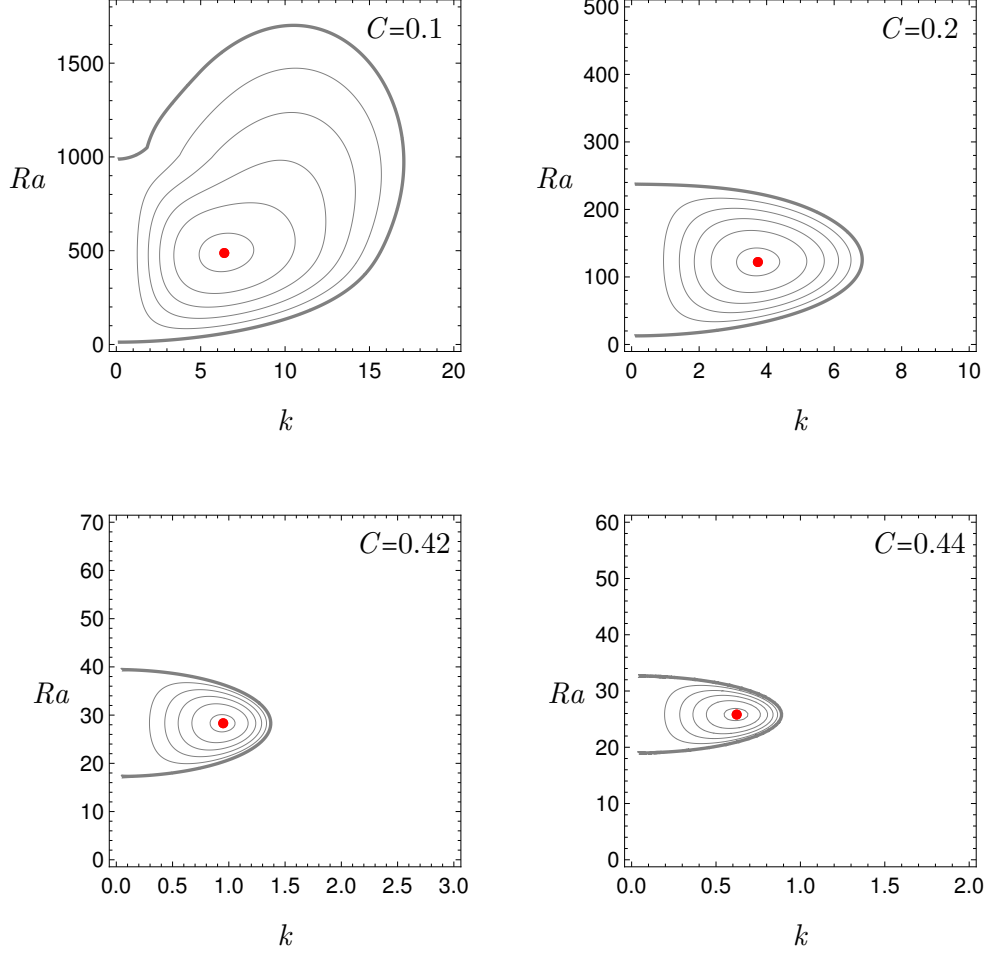


Figure 13: Same as Fig. 12 but for $\phi = \pi/2$. $\text{Im}[\omega] = 144.045$ at $Ra = 487.596$ and $k = 6.39767$ for $C = 0.1$, $\text{Im}[\omega] = 17.9898$ at $Ra = 122.111$ and $k = 3.74012$ for $C = 0.2$, $\text{Im}[\omega] = 0.0782786$ at $Ra = 28.3118$ and $k = 0.950117$ for $C = 0.42$ and $\text{Im}[\omega] = 0.0144728$ at $Ra = 25.8143$ and $k = 0.622522$ for $C = 0.44$.

7. Conclusions

Natural convection in a horizontal porous layer bounded by isoflux impermeable boundaries has been investigated. The imposed wall flux heating at the lower boundary coincides with the wall flux cooling at the upper boundary, so that no net heating or cooling of the saturated porous layer occurs.

The isoflux Darcy–Bénard instability arising in this system has been investigated from a novel perspective. Instead of focussing on the conduction basic state, endowed with a uniform vertical temperature gradient, we considered a one-parameter class of basic states compatible with the imposed boundary conditions. The parameter labelling the different states in this class is the dimensionless horizontal temperature gradient in the x direction, C , whose value is not constrained by the boundary conditions. The classical conduction basic state is included in the one-parameter class and corresponds to $C = 0$. When $C \neq 0$, the basic states feature infinitely wide Hadley cells with a zero mean horizontal flow rate across the layer. For this class of basic states, the thermal instability arises when the Rayleigh number, Ra , proportional to the imposed wall heat flux, is within the neutral stability threshold.

By adopting a linear stability analysis, the threshold condition has been expressed through neutral stability curves in the parametric (k, Ra) plane, where k is the wave number of each single normal mode

of perturbation. Since the neutral curves form closed loops when $C > 0$, the maximum and minimum Ra points of such curves yield the critical conditions, (k_c, Ra_c) . The orientation of the perturbation mode wave vector relative to the horizontal temperature gradient is parametrised with the angle ϕ . This angle expresses the inclination of the mode wave vector with respect to the x axis. Then, $\phi = 0$ describes a situation where the normal mode propagates in the x direction, i.e. it defines the transverse rolls. Longitudinal rolls are then given by $\phi = \pi/2$ and intermediate values of ϕ yield oblique rolls. The main features of the linear stability analysis are the following:

- For $C = 0$, the well-known results for the classical conduction basic state have been retrieved. The orientation angle ϕ does not influence the transition to instability. The critical condition happens with $k_c = 0$ and $Ra_c = 12$ and a vanishing angular frequency.
- For $C \neq 0$, the longitudinal rolls ($\phi = \pi/2$) are the most unstable modes at onset of the instability, with the critical condition being triggered by infinite wavelength modes ($k_c = 0$) from below. The same is true from above when C is large enough. Otherwise, finite wavelength modes $k_c \neq 0$ trigger the onset of instability.
- For $C \neq 0$, neutrally stable longitudinal modes are always stationary, while oblique and transverse rolls ($0 \leq \phi < \pi/2$) can be either stationary or travelling. In other words, their angular frequency can be either zero or nonzero.
- The lower critical value of Ra_c is determined analytically for every C and is a monotonic increasing function of C . Thus, the most unstable instance within the one-parameter class of basic states is $C = 0$. Its upper counterpart can only be determined analytically for large enough C .
- For $C = 0$, the neutral stability curve yields a monodromic function $Ra(k)$ which is monotonic increasing and defined for every $k \geq 0$.
- For $C \neq 0$, the neutral stability curves yield polydromic functions $Ra(k)$. Such curves display, roughly speaking, the shape of a horseshoe and they are confined to wave numbers k bounded by maximum values where turning points exist.

We finally point out that, considering the novelty of the present study, further investigations deserve to be undertaken in order to better understand the stability of this class of basic states. In particular, we mention the transition to absolute instability, the dynamics of spatial modes and the nonlinear development of the disturbances as possible tasks for a future work.

Acknowledgements

The authors A. Barletta and M. Celli acknowledge the financial support from the grant PRIN 2017F7KZWS provided by the Italian Ministry of Education and Scientific Research. The author P. V. Brandão acknowledges the financial support from Coordenação de Aperfeiçoamento de Pessoal de Nível Superior - Brasil (CAPES) - Grant nº 88881. 174085/2018-01

References

- [1] D. A. S. Rees, The stability of Darcy-Bénard convection, in: K. Vafai, H. A. Hadim (Eds.), Handbook of Porous Media, CRC Press, New York, 2000, pp. 521–558.
- [2] P. A. Tyvand, Onset of Rayleigh-Bénard convection in porous bodies, in: D. B. Ingham, I. Pop (Eds.), Transport Phenomena in Porous Media II, Pergamon, New York, 2002, pp. 82–112.
- [3] B. Straughan, Stability and Wave Motion in Porous Media, Springer, 2010.

- [4] A. Barletta, Thermal instabilities in a fluid saturated porous medium, in: A. Öchsner, G. E. Murch (Eds.), *Heat Transfer in Multi-Phase Materials*, Springer, New York, 2011, pp. 381–414.
- [5] D. A. Nield, A. Bejan, *Convection in Porous Media*, Springer, New York, NY, 5 edition, 2017.
- [6] A. Barletta, *Routes to Absolute Instability in Porous Media*, Springer, New Yourk, NY, 2019.
- [7] P. G. Drazin, W. H. Reid, *Hydrodynamic Stability*, Cambridge University Press, 2004.
- [8] D. A. Nield, Onset of thermohaline convection in a porous medium, *Water Resources Research* 4 (1968) 553–560.
- [9] A. Barletta, D. A. S. Rees, Local thermal non-equilibrium effects in the Darcy-Bénard instability with isoflux boundary conditions, *International Journal of Heat and Mass Transfer* 55 (2012) 384–394.
- [10] G. Hadley, Vi. Concerning the cause of the general trade-winds, *Philosophical Transactions of the Royal Society of London* 39 (1735) 58–62.
- [11] H. F. Diaz, R. S. Bradley, The Hadley circulation: present, past, and future, in: H. F. Diaz, R. S. Bradley (Eds.), *The Hadley Circulation: Present, Past and Future*, Springer, 2004, pp. 1–5.
- [12] J. E. Weber, Convection in a porous medium with horizontal and vertical temperature gradients, *International Journal of Heat and Mass Transfer* 17 (1974) 241–248.
- [13] D. A. Nield, Convection in a porous medium with inclined temperature gradient and horizontal mass flow, in: G. Hetsroni (Ed.), *Heat Transfer 1990: Proceedings of the Ninth International Heat Transfer Conference*, Jerusalem, Israel, vol. 5, Hemisphere, 1990, pp. 153–158.
- [14] D. A. Nield, Convection in a porous medium with inclined temperature gradient, *International Journal of Heat and Mass Transfer* 34 (1991) 87–92.
- [15] D. A. Nield, D. M. Manole, J. L. Lage, Convection induced by inclined thermal and solutal gradients in a shallow horizontal layer of a porous medium, *Journal of Fluid Mechanics* 257 (1993) 559–574.
- [16] D. A. Nield, Convection in a porous medium with inclined temperature gradient: additional results, *International Journal of Heat and Mass Transfer* 37 (1994) 3021–3025.
- [17] D. M. Manole, J. L. Lage, D. A. Nield, Convection induced by inclined thermal and solutal gradients, with horizontal mass flow, in a shallow horizontal layer of a porous medium, *International Journal of Heat and Mass Transfer* 37 (1994) 2047–2057.
- [18] D. M. Manole, J. L. Lage, Numerical simulation of supercritical Hadley circulation, within a porous layer, induced by inclined temperature gradients, *International Journal of Heat and Mass Transfer* 38 (1995) 2583–2593.
- [19] P. N. Kaloni, Z. Qiao, Non-linear stability of convection in a porous medium with inclined temperature gradient, *International Journal of Heat and Mass Transfer* 40 (1997) 1611–1615.
- [20] D. A. Nield, Convection in a porous medium with inclined temperature gradient and vertical through-flow, *International Journal of Heat and Mass Transfer* 41 (1998) 241–243.
- [21] L. Brevdo, M. Ruderman, On the convection in a porous medium with inclined temperature gradient and vertical throughflow. Part I. Normal modes, *Transport in Porous Media* 80 (2009) 137–151.
- [22] L. Brevdo, M. Ruderman, On the convection in a porous medium with inclined temperature gradient and vertical throughflow. Part II. Absolute and convective instabilities, and spatially amplifying waves, *Transport in Porous Media* 80 (2009) 153–172.

- [23] L. Brevdo, Three-dimensional absolute and convective instabilities at the onset of convection in a porous medium with inclined temperature gradient and vertical throughflow, *Journal of Fluid Mechanics* 641 (2009) 475–487.
- [24] A. Barletta, D. A. Nield, Instability of Hadley-Prats flow with viscous heating in a horizontal porous layer, *Transport in Porous Media* 84 (2010) 241–256.
- [25] A. Barletta, M. Celli, A. V. Kuznetsov, Heterogeneity and onset of instability in Darcy’s flow with a prescribed horizontal temperature gradient, *ASME Journal of Heat Transfer* 134 (2012) 042602 (8 pages).
- [26] M. Schuabb, L. S. de B. Alves, S. da C. Hirata, Two-and three-dimensional absolute instabilities in a porous medium with inclined temperature gradient and vertical throughflow, *Transport in Porous Media* 132 (2020) 135–155.
- [27] S. Kimura, M. Vynnycky, F. Alavyoon, Unicellular natural circulation in a shallow horizontal porous layer heated from below by a constant flux, *Journal of Fluid Mechanics* 294 (1995) 231–257.
- [28] J. P. Boyd, *Chebyshev and Fourier Spectral Methods*, Dover, New York, NY, 2001.
- [29] M. P. Juniper, A. Hanifi, V. Theofilis, Modal stability theory, *Applied Mechanics Reviews* 66 (2014).
- [30] G. I. El-Baghdady, M. El-Azab, Chebyshev–Gauss–Lobatto pseudo–spectral method for one–dimensional advection–diffusion equation with variable coefficients, *Sohag Journal of Mathematics* 3 (2016) 7–14.
- [31] A. Gueye, M. N. Ouarzazi, S. da C. Hirata, H. B. Hamed, Onset of primary and secondary instabilities of viscoelastic fluids saturating a porous layer heated from below by a constant flux, *Fluids* 2 (2017) 42.
- [32] L. Kalla, M. Mamou, P. Vasseur, L. Robillard, Multiple steady states for natural convection in a shallow porous cavity subject to uniform heat fluxes, *International Communications in Heat and Mass Transfer* 26 (1999) 761–770.
- [33] E. Anderson, Z. Bai, C. Bischof, L. S. Blackford, J. Demmel, J. Dongarra, J. Du Croz, A. Greenbaum, S. Hammarling, A. McKenney, et al., *LAPACK Users’ Guide*, SIAM, Philadelphia, PA, 1999.
- [34] L. S. de B. Alves, S. da C. Hirata, M. N. Ouarzazi, Linear onset of convective instability for rayleigh–bénard–couette flows of viscoelastic fluids, *Journal of Non-Newtonian Fluid Mechanics* 231 (2016) 79–90.
- [35] L. S. de B. Alves, S. da C. Hirata, M. Schuabb, A. Barletta, Identifying linear absolute instabilities from differential eigenvalue problems using sensitivity analysis, *Journal of Fluid Mechanics* 870 (2019) 941–969.

Appendix A. Small- C asymptotic solution

It is possible to reduce the $O(C^0)$ solution of Eq. (17) to a dispersion relation which gives $\tilde{R}a_0$ as an implicit function of k . Given that the equation for $\tilde{T}_0(z)$ is of linear constant-coefficient type, a substitution of

$$\tilde{T}_0(z) = e^{bz} \tag{A.1}$$

leads to the characteristic equation

$$k^4 + b^4 - k^2(\tilde{R}a_0 + 2b^2) = 0, \tag{A.2}$$

for which solutions are given by $b = \pm b_1$ and $b = \pm b_2$, with

$$b_1 = \left(k^2 - k\tilde{R}a_0^{1/2}\right)^{1/2}, \tag{A.3}$$

and

$$b_2 = \left(k^2 + k\tilde{R}a_0^{1/2} \right)^{1/2}, \quad (\text{A.4})$$

and the general solution for \tilde{T}_0 is written as

$$\tilde{T}_0(z) = m_1 e^{-b_1 z} + m_2 e^{b_1 z} + m_3 e^{-b_2 z} + m_4 e^{b_2 z}. \quad (\text{A.5})$$

On applying the appropriate boundary conditions that can be retrieved from Eqs. (10) the values of the coefficients, m_1 to m_4 , may be shown to satisfy the matrix/vector equation,

$$\begin{bmatrix} -b_1 & b_1 & -b_2 & b_2 \\ -b_1 e^{-b_1} & b_1 e^{b_1} & -b_2 e^{-b_2} & b_2 e^{b_2} \\ b_1^2 - k^2 & b_1^2 - k^2 & b_2^2 - k^2 & b_2^2 - k^2 \\ b_1^2 e^{-b_1} - e^{-b_1} k^2 & b_1^2 e^{b_1} - e^{b_1} k^2 & b_2^2 e^{-b_2} - e^{-b_2} k^2 & b_2^2 e^{b_2} - e^{b_2} k^2 \end{bmatrix} \begin{bmatrix} m_1 \\ m_2 \\ m_3 \\ m_4 \end{bmatrix} = 0. \quad (\text{A.6})$$

Nonzero solutions correspond to when the determinant of the matrix is equal to zero.

For the higher order equations, the general solution should have the same form as that at zero order, and we consider a particular solution of the form

$$\tilde{T}_j^{(p)}(z) = M_1 m_1 z e^{-b_1 z} + M_2 m_2 z e^{b_1 z} + M_3 m_3 z e^{-b_2 z} + M_4 m_4 z e^{b_2 z}, \quad (\text{A.7})$$

which by applying on the equation of j -th order is possible to recover the expressions for the M coefficients.